MITF deficiency accelerates GNAQ-driven uveal melanoma

Grace B. Phelps[a,b,1] (ORCID), Hannah R. Hagen[a,b,1] (ORCID), Adam Amsterdam[a,b] (ORCID), and Jacqueline A. Lees[a,b,2]

Cutaneous melanoma (CM) and uveal melanoma (UM) both originate from the melanocytic lineage but are primarily driven by distinct oncogenic drivers, *BRAF/NRAS* or *GNAQ/GNA11*, respectively. The melanocytic master transcriptional regulator, MITF, is essential for both CM development and maintenance, but its role in UM is largely unexplored. Here, we use zebrafish models to dissect the key UM oncogenic signaling events and establish the role of MITF in UM tumors. Using a melanocytic lineage expression system, we showed that patient-derived mutations of GNAQ ($GNAQ^{Q209L}$) or its upstream CYSLTR2 receptor ($CYSLTR2^{L129Q}$) both drive UM when combined with a cooperating mutation, $tp53^{M214K/M214K}$. The tumor-initiating potential of the major GNAQ/11 effector pathways, YAP, and phospholipase C-β (PLCβ)–ERK was also investigated in this system and thus showed that while activated YAP (YAP^{AA}) induced UM with high potency, the patient-derived PLCβ4 mutation ($PLCB4^{D630Y}$) very rarely yielded UM tumors in the $tp53^{M214K/M214K}$ context. Remarkably, *mitfa* deficiency was profoundly UM promoting, dramatically accelerating the onset and progression of tumors induced by $Tg(mitfa:GNAQ^{Q209L});tp53^{M214K/M214K}$ or $Tg(mitfa:CYSLTR2^{L129Q});tp53^{M214K/M214K}$. Moreover, *mitfa* loss was sufficient to cooperate with $GNAQ^{Q209L}$ to drive *tp53*–wild type UM development and allowed $Tg(mitfa:PLCB4^{D630Y});tp53^{M214K/M214K}$ melanocyte lineage cells to readily form tumors. Notably, all of the $mitfa^{-/-}$ UM tumors, including those arising in $Tg(mitfa:PLCB4^{D630Y});tp53^{M214K/M214K};mitfa^{-/-}$ zebrafish, displayed nuclear YAP while lacking hyperactive ERK indicative of PLCβ signaling. Collectively, these data show that YAP signaling is the major mediator of UM and that *MITF* acts as a bona fide tumor suppressor in UM in direct opposition to its essential role in CM.

uveal | melanoma | mitf | zebrafish

Uveal melanoma (UM) is the most common adult cancer of the eye, although still relatively rare (1). The primary tumors are readily treatable by surgical removal of the eye and/or radiation therapy, but ~50% of patients develop liver metastases for which there is no Food and Drug Administration–approved treatment (1–3). UM arises in the choroid, iris, or ciliary body through the transformation of resident melanocytes. Due to their shared cell of origin, UM is frequently compared to cutaneous melanoma (CM), which is more prevalent and thus more extensively studied. CM affects 200 per 1,000,000 people in the United States (4), and it is the deadliest form of skin cancer due to the aggressive, metastatic nature of CM tumors. Recent advances in therapies, such as immune checkpoint therapy and targeted therapies, have led to significant improvements in CM patient outcomes (5). Unfortunately, therapies with positive outcomes in CM have little or no effect in slowing the metastatic progression of UM, demonstrating fundamental differences between CM and UM despite their shared cell of origin (3).

One potential explanation for the differences in therapy efficacy between CM and UM is the fact that they have different initiating mutational events. CM is typically driven by oncogenic mutations in *BRAF* or *NRAS*, which lead to activation of the MEK/ERK signaling cascade (6, 7). In contrast, greater that 80% of UM cases are driven by oncogenic mutations $GNAQ^{Q209L}$ or $GNA11^{Q209L}$, herein referred to as *GNAQ/11*, which encode the α subunits of the G protein heterotrimeric receptors (8). A small subset of UM cases lack GNAQ/11 mutations and instead carry an activating mutation in the upstream G protein–coupled receptor CYSLTR2 ($CYSLTR2^{L129Q}$; 3%), reinforcing the importance of this signaling complex (8–10). GNAQ/11 signals to a variety of downstream pathways, including phospholipase C-β (PLCβ) and YAP. In UM, PLCβ has been shown to activate two PKC isoforms δ and ε, which then induce the Ras-GEF RasGRP3 to activate Ras downstream pathways, including the MEK/ERK axis that is so important in CM (11, 12). Additionally in UM, oncogenic GNAQ/11 triggers the nuclear localization of YAP through a noncanonical, Hippo-independent mechanism that involves Trio/Rho/Rac/FAK (13–15). Nuclear

Significance

Uveal melanoma (UM) is a cancer of eye melanocytes. Although relatively rare, UM is extremely deadly, as approximately half of all patients develop liver metastases for which there are no approved therapies. Even therapies that succeed in cutaneous melanoma (CM) treatment have proven ineffectual for UM, highlighting both the distinct nature of these two melanomas and the need to understand the differences between them. Here, we show that autochthonous UM tumors are rapidly induced by activated YAP and can lack hyperactive ERK, highlighting YAP as a promising therapeutic target. We further show that *MITF* functions as a tumor suppressor in UM in contrast to its essential role in CM, establishing that MITF inhibition should not be entertained for UM treatment.

YAP is able to bind to the transcriptional enhanced associated domain (TEAD) transcription factors and activate a downstream transcriptional program that promotes cell growth and proliferation (16).

Various biochemical, genetic, and therapeutic observations provide arguments for and against the importance of PLCβ versus YAP arms of the GNAQ/11 pathway in UM. A small subset of UM patients lack *GNAQ/11* or *CYSLTR2* mutations and instead carry an activating D630Y mutation in the PLCβ isoform *PLCB4* (3 to 7%) (17, 18). This offers a compelling genetic argument that the PLCβ axis is a key driver of tumorigenesis in UM. However, this notion is challenged by the finding that inhibitors of the PKC/MEK/ERK axis are ineffective in the clinic (2, 19, 20), raising the possibility that PKC/MEK/ERK signaling is not as important in UM and/or that PLCβ promotes tumorigenesis through an alternate pathway or pathways. YAP is never mutated in UM or in any other tumor type, but many UM tumors display activated, nuclear-localized YAP (13, 14). Moreover, knockdown of YAP was found to suppress the proliferation of UM cell lines and their ability to form tumors in xenograft assays (13–15), and activated YAP, but not oncogenic KRAS, was shown to induce murine uveal melanocytes to form tumors in vivo (21). Challenging these observations is a recent study of primary UM patient samples, which showed that a subset has little or no nuclear YAP staining and reported no correlation between patient survival and nuclear YAP expression (22). Thus, there is still debate in the field as to which of these pathways is most important for the tumorigenic potential of GNAQ/11.

There is also strong rationale to establish the role of MITF in UM. MITF is on chromosome 3, and monosomy 3 correlates with poor UM prognosis (23). MITF is a transcription factor that directly activates genes that regulate melanocyte differentiation, proliferation, and survival (24), and it enables the proper migration and specification of melanocytes during development as well as maintenance of the adult melanocyte pool (25). Many of the MITF downstream transcriptional programs also influence cancer initiation and progression, and, accordingly, MITF has been shown to play an important role in CM. In this context, MITF's influence is highly dependent on its expression level (26, 27), with high, intermediate, or low levels being associated with more differentiated, proliferative, or invasive tumor phenotypes, respectively (26–28). Moreover, by modulating their MITF expression, CM cells are able to shift between these various states to enable tumor growth versus invasion and metastasis (29–31) and also alter sensitivity to targeted therapies, such and BRAF and MEK inhibitors (32, 33). This plasticity in MITF expression, dubbed the rheostat model, has been well documented in CM cell lines, patient samples, and both murine and zebrafish CM models (34–36). Additionally, genetic approaches have unequivocally established that complete loss of MITF is sufficient to prevent CM formation and even achieve tumor regression, indicating that CM is lineage addicted to MITF (34, 37). Remarkably, despite the central role of MITF in CM, the role of MITF in UM remains largely unexplored.

Zebrafish have a high degree of genetic homology to humans and have been used to study a variety of human cancers, including CM (38, 39). Our laboratory previously developed a model of UM by expressing human *GNAQ^{Q209L}* under the control of the *mitfa* promoter (40). In this model, we found that *GNAQ^{Q209L}* expression led to profound changes in the properties of melanocytes within a few days of development, but tumors developed only rarely and with late onset (40).

When the *GNAQ^{Q209L}* transgene was combined with a mutant *tp53* allele, the zebrafish develop UM with complete penetrance (40). In this current study, we use zebrafish to assess the role of MITF and the relative contributions of GNAQ downstream pathway components in driving UM tumorigenesis.

Results

mitfa Loss Accelerates GNAQ^{Q209L}-Mediated Tumorigenesis in a Zebrafish Model of UM. Our first goal was to compare the effects of MITF deficiency in UM versus CM using zebrafish models. Previous studies, and our own observations, unequivocally demonstrated that combining inactivating alleles of the zebrafish homolog of MITF, *mitfa^{w2/w2}* (henceforth simplified to *mitfa^{-/-}* or m−) (41), with the zebrafish CM model, *Tg(mitfa:BRAF^{V600E});tp53^{M214K/M214K}* (with *tp53^{M214K/M214K}*, henceforth simplified to *tp53^{-/-}*) (38), completely blocks CM tumor formation (42). To verify that the lack of tumorigenesis in *Tg(mitfa:BRAF^{V600E});tp53^{-/-};mitfa^{-/-}* zebrafish was not merely caused by an absence of oncogene-expressing cells in the melanocyte lineage due to *mitfa* mutation, we introduced a *mitfa:GFP* reporter into *Tg(mitfa:BRAF^{V600E});tp53^{-/-};mitfa^{-/-}* zebrafish and showed that numerous cells express green fluorescent protein (GFP; *SI Appendix,* Fig. S1). The complete absence of CM formation in *Tg(mitfa:BRAF^{V600E});tp53^{-/-};mitfa^{-/-}* zebrafish and the regression of tumors in *Tg(mitfa:BRAF^{V600E});tp53^{-/-}* zebrafish with a temperature-sensitive *mitfa* (34) showed that BRAF^{V600E}-driven CM cannot tolerate loss of *mitfa*. Given this, we asked whether *mitfa* loss is also incompatible with oncogenic GNAQ-driven tumorigenesis. For this, we crossed our existing *Tg(mitfa:GNAQ^{Q209L});tp53^{-/-}* Q-1 UM model (40) into the *mitfa^{-/-}* background. Herein, for simplicity, we will refer to the resulting lines as Qpm+ and Qpm−, respectively. Strikingly, *mitfa* loss was entirely compatible with tumor formation in Qpm− zebrafish (Fig. 1A). Qpm− tumors arose in the eye, skin, and abdomen, as we previously found for Qpm+ tumors (40) (*SI Appendix,* Fig. S2A), but they were typically unpigmented (Fig. 1B). Qpm+ had a higher incidence of skin tumors and a lower incidence of internal tumors than Qpm−, while eye tumors were observed at similar frequency in these two genotypes (*SI Appendix,* Fig. S2A). The tumor burden was similar between Qpm+ and Qpm− at the time of death (*SI Appendix,* Fig. S2B). However, the absence of *mitfa* caused noticeable changes in the tumor histopathology; Qpm− tumors had a more homogeneous dedifferentiated morphology and tightly packed nuclei, and they were typically much more invasive (even invading into the brain) than their Qpm+ counterparts (*SI Appendix,* Fig. S3). Consistent with this increase in aggressiveness, *mitfa* loss was not simply compatible with UM formation but actually greatly accelerated tumor formation. *mitfa^{-/-}* also impacted the formation of malignant peripheral nerve sheath tumors (MPNSTs) (Fig. 1A), which are the hallmark tumor type of both *tp53^{-/-}* (pm+) and *mitfa^{-/-};tp53^{-/-}* (pm−) controls. However, *mitfa^{-/-}* had a greater impact on GNAQ^{Q209L}-driven tumorigenesis, with the change in median survival being 2.5-fold for Qpm− versus Qpm+ compared to only 1.4-fold for pm− versus pm+. Thus, *mitfa^{-/-}* accelerates GNAQ^{Q209L} tumorigenesis even when considering the reduced survival of pm− zebrafish.

We wanted to be sure that the Qpm− tumor phenotype was not simply an artifact of the GNAQ^{Q209L} transgene itself (e.g., unique to its integration site). Thus, we also crossed two independent GNA11^{Q209L} lines (herein referred to as "11" lines)
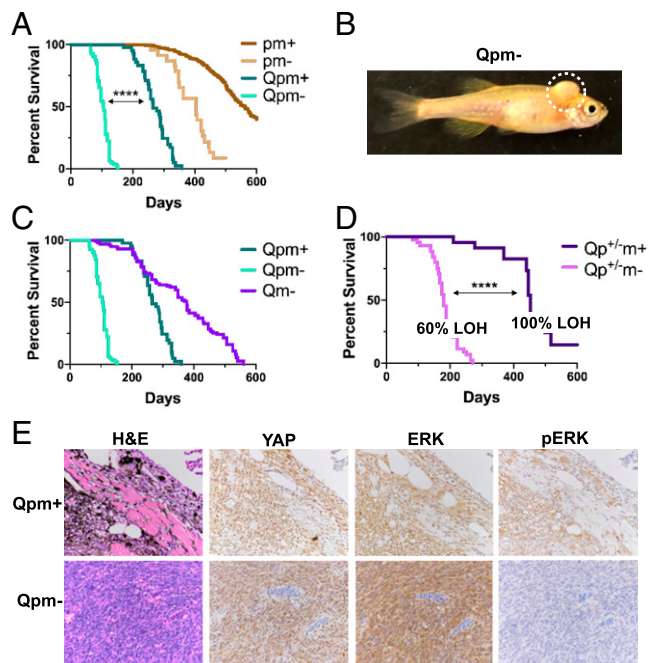
Fig. 1. Mitfa loss accelerates GNAQ^{Q209L}-driven tumorigenesis, and resulting tumors stain negatively for hyperactive ERK; Q, *Tg(mitfa:GNAQ^{Q209L})*; p, *tp53$^{M214K/M214K}$*; m+, *mitfa$^{+/+}$*; m−, *mitfa$^{-/-}$*; p$^{+/-}$, *tp53$^{+/M214K}$*. (*A*) Kaplan–Meier curves for the indicated genotypes show that overall survival of *Tg(mitfa:GNAQ^{Q209L})*-expressing zebrafish was significantly decreased by *mitfa* deficiency (P < 0.0001, determined by log-rank test). The pm+ and pm− zebrafish develop MPNSTs, while Qpm+ and Qpm− zebrafish develop UMs and, less frequently, MPNSTs. (*B*) A representative image, with tumor outlined by dotted line, shows the typical unpigmented UM tumor phenotype of Qpm− zebrafish. (*C*) Kaplan–Meier curves show that *mitfa$^{-/-}$* also cooperates with GNAQ^{Q209L} to decrease overall survival in a *tp53*-WT background. The Qpm+ and Qpm− curves from *A* are included for comparison. (*D*) Kaplan–Meier curves showing that Qp$^{+/-}$m− zebrafish have significantly reduced survival compared to Qp$^{+/-}$m+ counterparts (P < 0.0001, determined by log-rank test) as well as a reduced reliance on *tp53* LOH, as determined by DNA sequencing of the mutation-bearing *tp53* exon of excised tumors. (*E*) Representative images (*n* ≥ 3 for each stain and genotype) of hematoxylin and eosin (H&E) and IHC for YAP, ERK1/2, and phospho-ERK1/2 (pERK; active) for Qpm+ and Qpm− tumors. YAP activation was detected through nuclear localization.

into the pm− background and found that these lines also displayed accelerated tumor formation in pm− versus pm+ contexts (*SI Appendix*, Fig. S4). Thus, we conclude that accelerated tumor formation resulting from *mitfa* deficiency is a hallmark of oncogenic GNAQ/11 signaling. Herein, we will refer to all GNAQ/11 pathway–driven tumors as UM, regardless of their *mitfa* status.

Given the greatly accelerated rate of UM tumorigenesis in Qpm− versus Qpm+ zebrafish, we wondered whether deletion of *mitfa* alone (i.e., in a *tp53*–wild type (WT) context) might be sufficient to cooperate with oncogenic GNAQ/11. We generated Qm− and 11m− lines and found that both developed tumors with high penetrance (Fig. 1*C* and *SI Appendix*, Fig. S4), in clear contrast to Qm+ or 11m+ zebrafish, which develop UM tumors only rarely and with long latency (40). Moreover, Qm− zebrafish that were heterozygous for *tp53* showed accelerated UM formation and reduced dependence on *tp53* loss of heterozygosity (LOH; LOH 60% of tumors; Fig. 1*D*) compared to Qm+; *tp53$^{+/-}$* controls (LOH 100% of tumors; Fig. 1*D*). Notably, Qpm− and Qm− UM displayed nearly identical histopathological features, and both were typically unpigmented, dedifferentiated, and highly invasive (*SI Appendix*, Fig. S3). We noticed that Qpm− and Qm− zebrafish occasionally developed black pigment patches or

black-appearing tumors in adulthood, which suggested that GNAQ^{Q209L} can occasionally reactivate pigment synthesis genes in the absence of *mitfa* coding sequence (*SI Appendix*, Fig. S5A). However, in most cases, the tumors did not arise from the black pigment patches (*SI Appendix*, Fig. S5A). Moreover, pigmented and unpigmented Qm− tumors had similar histology and overall survival kinetics (*SI Appendix*, Figs. S5B and S6). Thus, we conclude that the observed reactivation of pigment synthesis genes is not required for UM tumors and that *mitfa* is a bona fide tumor suppressor in this context.

Accelerated GNAQ^{Q209L}-Driven Tumorigenesis Lacks Hyperactive ERK Staining. We next expanded our analysis of GNAQ^{Q209L}-driven tumor phenotypes to determine the activation status of GNAQ/11 downstream signaling pathways in established tumors. Because GNAQ is known to activate both YAP and MEK/ERK signaling, we performed immunohistochemistry (IHC) on tumors to screen for nuclear YAP and phosphorylated ERK. Our previous work (40) and this study (Fig. 1*E*) demonstrate that Qpm+ UM display active, nuclear-localized YAP, mirroring findings in many patient samples. Our current analyses showed that Qpm+ UM also displayed heterogeneous activation of MEK/ERK, as evidenced by positive staining for phospho-ERK (Fig. 1*E*). Quantification using QuPath software determined that the average percentage of phospho-ERK– positive tumor cells in Qpm+ tumors (*n* = 4) was 42.93% ± 9.95% (*SI Appendix*, Fig. S7). Thus, these findings confirmed that GNAQ activates both downstream signaling axes in the *mitfa*-WT state.

We then asked whether Qpm− UM displayed similar activation of downstream signaling pathways by again staining for YAP and phospho-ERK. Remarkably, Qpm− and Qm− tumors displayed strong YAP$^+$ nuclei (Fig. 1*E*), but only 0.56% ± 0.47% of the cells (*n* = 4 tumors) scored as phospho-ERK positive (Fig. 1*E* and *SI Appendix*, Fig. S7). We also obtained one pigmented Qm− tumor for IHC and found that it was similarly positive for nuclear YAP and largely negative for phospho-ERK (0.62% of tumor cells; *SI Appendix*, Fig. S8). These findings indicate the presence of widespread activation of YAP in both Qpm− and Qm− UM but show that the ERK signaling cascade is largely down-regulated in the *mitfa$^{-/-}$* tumors, raising the possibility that it might be dispensable for UM in the absence of *mitfa*.

RNA Sequencing and Phospho-Proteomics Determine That Qpm− Tumors Are Deficient in PLCβ4–PKCδ/ε Signaling and Up-Regulate MYC Target Genes. To gain a deeper understanding of the differences between Qpm+ and Qpm− tumors, we conducted bulk RNA sequencing on zebrafish tumors from various genotypes and anatomical locations, including 8 Qpm+ eye, 9 Qpm+ skin, 10 Qpm−, and 10 Qm− UM as well as 9 *Tg(mitfa:BRAF^{V600E});tp53$^{-/-}$* (Bpm+) CM for comparison (GSE190802). Initially, we performed principal component analysis (PCA; Fig. 2*A*). The Qpm+ tumors all clustered together, reinforcing the notion that the eye and skin tumors are not fundamentally different. Consequently, we considered these together for subsequent downstream analyses. Somewhat unexpectedly, the Qpm− and Qm− also clustered as a group, indicating that *tp53* status has little impact on the transcriptional profile of the GNAQ^{Q209L}-driven *mitfa$^{-/-}$* UM (Fig. 2*A*). Finally, the *mitfa*-positive and *mitfa*-negative UM tumors segregated from each another as well as from the BRAF^{V600E}-driven CM, arguing that they represent three distinct groups.
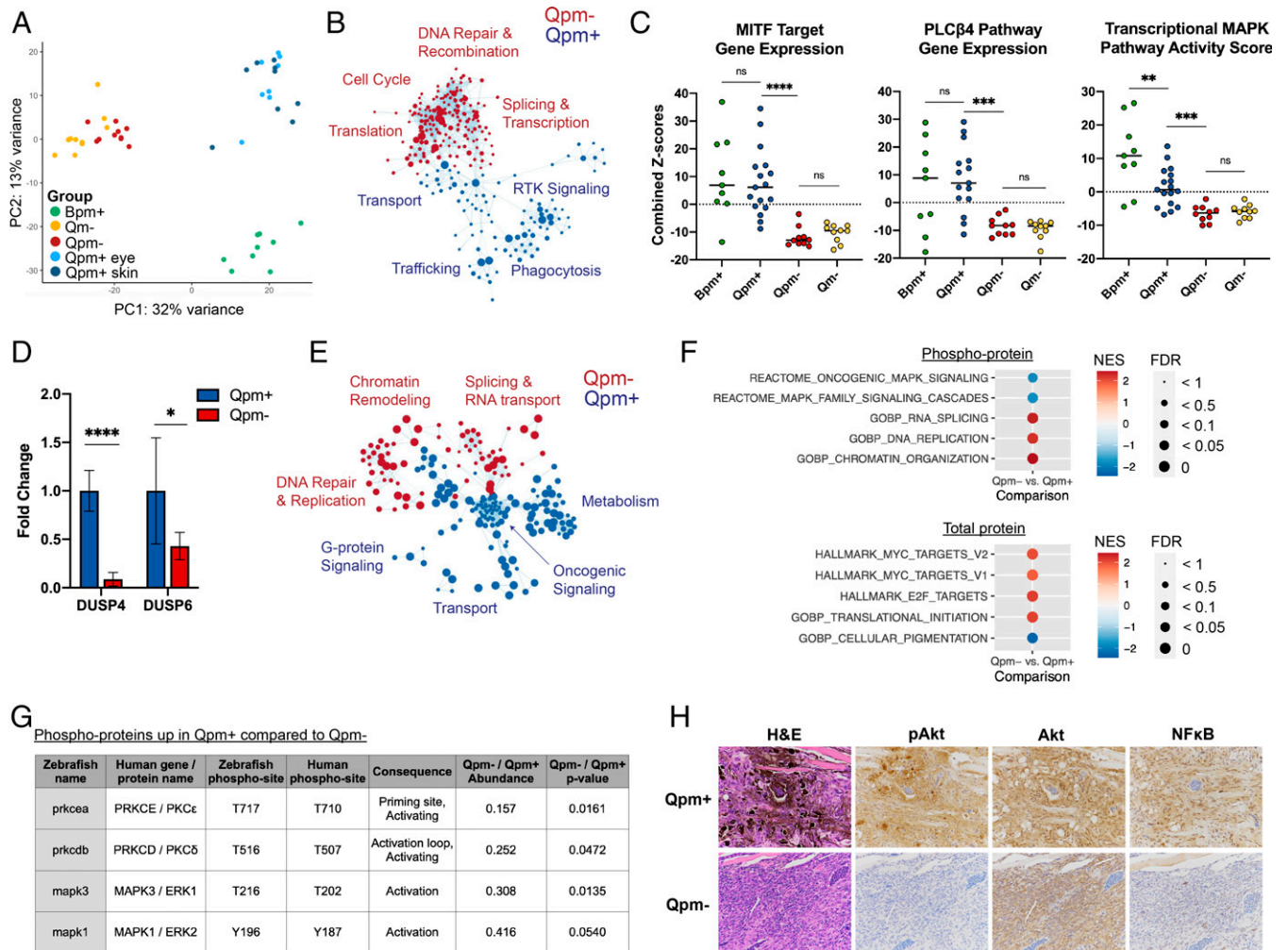
Fig. 2. RNA sequencing and phospho-proteomics determine that Qpm− tumors are deficient in PLCβ4–PKCδ/ε signaling and up-regulate MYC target genes. Genotype abbreviations are as indicated in Fig. 1; B, Tg(mitfa:BRAF^{V600E}). (A–C) RNA-sequencing data were generated for the following tumor numbers, genotypes, and tumor locations: 9 Bpm+, 8 Qpm+ eye, 9 Qpm+ skin, 10 Qpm−, and 10 Qm− (GSE190802). (A) PCA shows distinct clustering of Qpm+ tumors (regardless of their anatomical location), Qpm− and Qm− (regardless of tp53 status), and Bpm+. (B) Cytoscape enrichment map shows GSEA c2cp_Reactome data sets that were significantly enriched (false discovery rate [FDR] q value < 0.05) in Qpm− (red) versus Qpm+ (blue). Each circle denotes a gene set, circle size denotes the number of genes in each gene set, and clustering and line length is determined by similar genes within each gene set. Complete GSEA results are shown in Dataset S1. (C) For each individual Bpm+, Qpm+, Qpm−, and Qm− tumor, combined Z scores were calculated for the identified zebrafish orthologs for the MITF target gene (Left), PLCβ4 pathway (Middle), or MAPK transcriptional activity (Right) gene sets. The bar denotes the medians for each tumor type. Qpm− and Qm− tumors have significantly reduced expression compared with either Qpm+ or Bpm+ tumors in each of the three gene sets (P < 0.001, determined by Student's unpaired t test). (D) qRT-PCR for the top two differentially expressed genes in the MAPK transcriptional activity gene set, DUSP4 and DUSP6, on new Qpm+ and Qpm− tumor samples (n = 6 each). Results are normalized to ACTB2 expression. Fold change is relative to the average of the Qpm+ samples, with error bars indicating SD. P < 0.0001 for DUSP4 and P = 0.033 for DUSP6, as determined by Student's unpaired t test. (E–G) Phospho-peptides and total proteins from Qpm− and Qpm+ tumors (n = 5/genotype) were quantified by mass spectrometry, and GSEA was conducted (complete results are shown in Dataset S1). (E) Cytoscape enrichment map shows c2cp Reactome and c5 Biological Processes data sets significantly enriched (FDR q value < 0.05) in phospho-proteins from Qpm− (red) versus Qpm+ (blue) tumors. (F) Key gene sets identified as significantly different between Qpm− and Qpm+ for phospho-proteins (Top) or total protein (Bottom), demonstrating enrichment of MAPK signaling in Qpm+ and MYC and E2F targets in Qpm−; NES, normalized enrichment score. (G) Phospho-peptides associated with PKCδ, PKCε, ERK1, and ERK2 activation that were reduced in Qpm− compared with Qpm+. (H) Representative IHC images (from n ≥ 3 per stain and genotype) for phospho-Akt (p-AKT; active), total AKT, and NF-κB (with nuclear staining indicating the active form) show that Qpm− tumors are deficient for signaling from pathways other than MAPK downstream of PKC–RasGRP3.

To identify gene programs that distinguish the Qpm+ and Qpm− tumors, we performed gene set enrichment analysis (GSEA). The results are shown in Dataset S1, and the reoccurring processes are illustrated in the form of a Cytoscape enrichment map (Fig. 2B). This revealed enrichment of transport/trafficking gene sets, likely due to melanosome shuttling, and receptor tyrosine kinase signaling, which were partly due to MAPK pathway signaling events, in Qpm+ tumors (Fig. 2B, blue circles; Dataset S1). In contrast, Qpm− tumors were enriched for cell cycle, DNA repair, splicing, and translation gene sets (Fig. 2B, red circles; Dataset S1). To further explore these differences, we examined the expression levels of genes

within several key human gene lists by identifying the corresponding zebrafish orthologs and then calculating and summing their z scores for all of the Qpm+, Qpm−, Bpm+, and Qm− tumors. We began with MITF target genes (24) (Dataset S1) as a positive control and showed that these had significantly lower expression in both Qpm− (P < 0.0001) and Qm− (P < 0.0001) UM than in Qpm+ UM (Fig. 2 C, Left). We then curated a zebrafish list of genes in the GNAQ–PLCβ4 pathway (Dataset S1) and found that these were also significantly downregulated in both Qpm− (P = 0.0003) and Qm− (P = 0.0001) versus in Qpm+ UM (Fig. 2 C, Middle). As MEK/ERK is activated through the GNAQ–PLCβ4 pathway in UM,

this could contribute to the lack of phospho-ERK staining in Qpm− tumors. To more directly assess the activity of MEK/ERK, we also examined a transcriptional MAPK pathway activity signature that was shown to predict MAPK signaling across many different cancer types (43) (Dataset S1). Consistent with the reduced phospho-ERK in our $mitfa^{-/-}$ tumors, the combined z scores from this MAPK activity signature were significantly lower in Qpm− ($P = 0.0004$) and Qm− ($P = 0.0007$) than in Qpm+ (Fig. 2 C, $Right$). Notably, the Bpm+ tumors had a significantly higher MAPK pathway activity score than Qpm+ ($P = 0.006$) and Qpm− ($P < 0.0001$), highlighting the central importance of the MAPK pathway in BRAF^{V600E}-driven tumors (Fig. 2 C, $Right$). To extend our analyses, we quantified mRNA levels for the top two most differentially expressed transcriptional MAPK pathway activity genes DUSP4 and DUSP6 in new Qpm+ and Qpm− tumors ($n = 6$ for each genotype) via qRT-PCR. This confirmed significant down-regulation of DUSP4 ($P < 0.0001$) and DUSP6 ($P = 0.03$) in Qpm− tumors (Fig. 2D). Taken together, these data indicate both that GNAQ/11–PLCβ4 pathway components and MAPK transcriptional targets are down-regulated in the $mitfa^{-/-}$ UM tumors.

Given the differential activation of signaling pathways in Qpm+ versus Qpm− tumors, we decided to perform phosphoproteomics and total proteomics on 10 newly isolated Qpm+ and Qpm− tumors (Datasets S2 and S3). Paralleling our transcriptional analyses above, we performed GSEA on both phospho-proteins and total proteins to identify programs that are more abundant in Qpm+ than in Qpm− UM (Fig. 2 E and F and Dataset S1). A Cytoscape enrichment map of the phospho-proteins showed that Qpm− tumors were enriched for DNA repair, chromatin remodeling, and splicing gene sets, whereas Qpm+ tumors were enriched for G protein signaling and oncogenic signaling gene sets (Fig. 2E). Notably, MAPK signaling gene sets were included in the Qpm+-enriched phospho-proteins (Fig. 2 F, Top). Phosphorylation can have very different results on protein function depending on the specific phosphorylation site. Thus, we examined our phosphoproteomics dataset for specific GNAQ–PLCβ4 pathway phospho-peptides. We detected ERK1/MAPK3 and ERK2/MAPK1 phospho-peptides that correspond to known activating regulatory events, and both were at much lower levels in Qpm− than in Qpm+ tumors (Fig. 2G). Moreover, Qpm− tumors also displayed significantly reduced abundance of activating phospho-peptides from PKCδ and PKCε, which are downstream effectors of PLCβ4 (Fig. 2G). This suggests that the down-regulation of MAPK/ERK in Qpm− tumors may result from decreased signaling higher up the pathway, namely, at or above PLCβ4–PKCδ/ε activation. To explore this possibility, we performed IHC for other PLCβ4–PKCδ/ε downstream pathways and indeed found that Qpm− tumors were deficient for active Akt (phospho-Akt), despite maintaining comparable total Akt levels, and also lacked NF-κB and hyperactive MEK1/2 (phospho-MEK1/2; Fig. 2H and SI Appendix, Fig. S9).

Collectively, our molecular analyses show that Qpm− tumors are transcriptionally enriched for proliferation-associated programs, while paradoxically showing significant down-regulation of the PLCβ4–PKCδ/ε signaling arm at both the transcriptional and posttranslational levels compared to Qpm+. One explanation for this phenomenon, outside of a possible tumor-suppressive role for the PLCβ4–PKCδ/ε signaling arm, is up-regulation of an alternative signaling pathway. Notably, our RNA sequencing and proteomics analyses both

showed significant enrichment for MYC target genes as well as E2F target genes in Qpm− relative to Qpm+ (Fig. 2 F, $Bottom$, and SI Appendix, Fig. S10). Moreover, Qpm− tumors had significantly higher mRNA levels of the MYC ortholog mycb as well as significantly higher total protein levels or activating phospho-peptides for several key inducers of MYC activation, including cdk7, npm1a and npm1b, wdr5, and brd4 (SI Appendix, Fig. S11). Interestingly, prior work in CM established that c-MYC can compensate for the absence of MITF, specifically its role in transcription initiation but not melanocyte differentiation, in part through up-regulation of CDK7 (44). These findings raise the possibility that the $mitfa^{-/-}$ state accelerates GNAQ^{Q209L}-driven tumorigenesis in part through MYC activation.

A Zebrafish Overexpression System Determines That CYSLTR2^{L129Q}, YAP^{AA}, and PLCβ4^{D630Y} Can Drive UM Tumorigenesis.

Our analyses of the Qpm− tumors seemed to highlight YAP activation and deemphasize the likely contribution of the PLCβ4–PKCδ/ε arm. To complement these findings, we directly assessed the ability of different putative UM drivers to form UM in zebrafish. For this, we modified an existing Tol2-based vector system, called miniCoopR (42), to allow melanocyte lineage–specific expression in zebrafish of both GFP and a test gene of interest (GOI) under the control of antiparallel $mitfa$ promoters. Unlike the original miniCoopR vector, this vector, which we call GOI–GFP, does not express the $mitfa$ coding sequence. When injected into single-cell zebrafish embryos, GOI–GFP integrates mosaically into the genomes of recipient zebrafish, yielding coexpression of GFP and the GOI in a subset of cells in the melanocyte lineage. For simplicity, we will represent resulting mosaic zebrafish as "GOI"➤ "recipient genotype".

To validate this system, we injected GOI–GFP carrying either GFP only (Ctl) or GFP and GNAQ^{Q209L} into $tp53^{-/-}$ zebrafish embryos (Ctl➤pm+ and Q➤pm+, respectively). In both cases, the resulting zebrafish had GFP$^+$ cells. Moreover, consistent with the hyperpigmentation of germline $Tg(mitfa:GNAQ^{Q209L})$ zebrafish (40), we observed hyperpigmentation patches specifically in Q➤pm+, which correlated with GFP expression (Fig. 3A). We also injected these vectors into $tp53^{-/-}$; $mitfa^{-/-}$ zebrafish embryos to yield Q➤pm− and Ctl➤pm− mosaics. We then aged all four mosaic cohorts and examined their tumor phenotypes; 100% of the Ctl➤pm+ and the Ctl➤pm− succumbed to MPNSTs, the hallmark tumor type of the $tp53^{-/-}$ state. Importantly, these tumors arose with similar kinetics to MPNSTs in the pm+ or pm− contexts (Fig. 3B) and were negative for GFP. This establishes that the vector itself was not protumorigenic. In stark contrast, both Q➤pm+ and Q➤pm− zebrafish developed GFP$^+$ UM with kinetics that were remarkably similar to those of germline Qpm+ and Qpm−, respectively (Fig. 3B). Together, these data indicated that this system yields an accurate readout of tumorigenic capacity. For simplicity moving forward, we will call the GFP$^+$ mosaic-derived tumors UM.

We used our GOI–GFP system to more directly test the ability of different GNAQ pathway components to promote UM. First, we tested the tumorigenic potential of the CYSLTR2^{L129Q} mutation. This mutation was previously identified in ~20% of UM patient tumors that were WT for GNAQ/11 and shown to activate GNAQ signaling (10), but its tumorigenic potential has not been addressed in an autochthonous in vivo tumor model. We used the GOI–GFP system to introduce CYSLTR2^{L129Q} (abbreviated "C") into both $tp53^{-/-}$ and $tp53^{-/-}$;$mitfa^{-/-}$ embryos. In the $mitfa$-WT
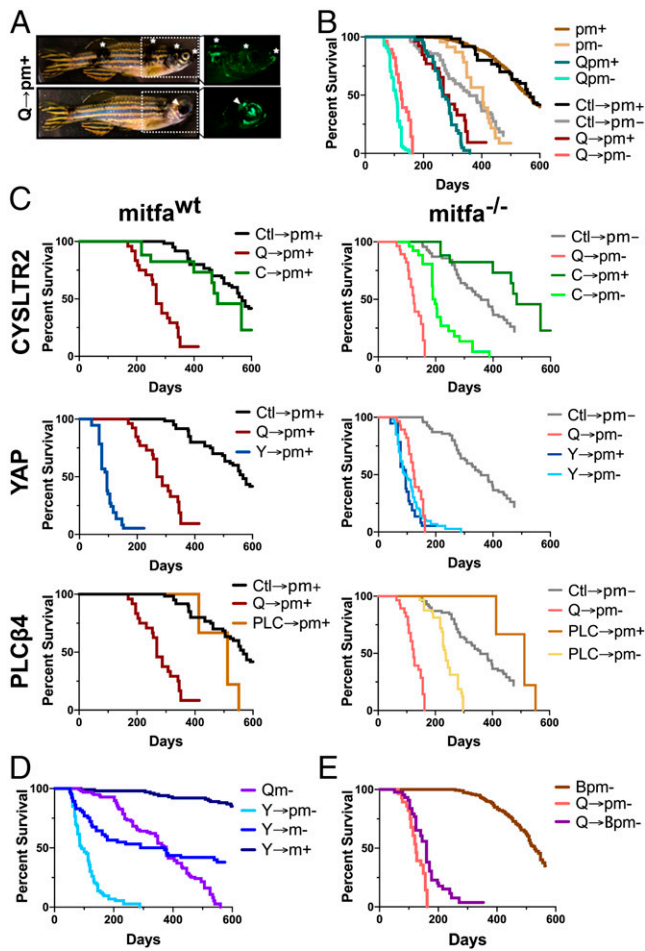
Fig. 3. A mosaic expression system determines that CYSLTR2^{L129Q}, YAP^{AA}, and PLCβ4^{D630Y} can drive UM tumorigenesis. Mosaic zebrafish are denoted by X➤Y, where X is the gene introduced, and Y is the recipient genotype; Ctl, control GOI–GFP vector; Q, *GNAQ*^{Q209L}; C, *CYSLTR2*^{L129Q}; Q, *GNAQ*^{Q209L}; Y, *YAP*^{AA}; PLC, *PLCB4*^{D630Y}. Germline zebrafish lines and recipient genotypes are as indicated in Figs. 1 and 2. (*A*) Representative zebrafish images confirm that introduction of GNAQ^{Q209L} via the GOI–GFP vector results in GFP$^+$ pigment patches and tumors. Asterisks and arrows denote pigment patches corresponding to GFP expression. (*B*) Kaplan–Meier curves show that mosaic zebrafish with control vector or GNAQ^{Q209L} introduced into pm+ or pm− recipients all have overall survivals that closely mirror their germline pm+, pm−, Qpm+, and Qpm− equivalents (*P* = n.s.). As with the germline mutants, Q➤pm+ versus Ctl➤pm+ and Q➤pm− versus Ctl➤pm− were both significantly different (*P* < 0.001, as determined by log-rank test). (*C*) Kaplan–Meier curves show the effects of mosaic expression of CYSLTR2^{L129Q}, YAP^{AA}, and PLCβ4^{D630Y} in *tp53*-mutant zebrafish that are either *mitfa*$^{+/+}$ (*Left*) or *mitfa*$^{-/-}$ (*Right*). Q➤pm+, Q➤pm−, Ctl➤pm+, and Ctl➤pm− data from *B* are shown for comparison. Statistical significance is as follows: CYSLTR2, C➤pm+ versus Ctl➤pm+ n.s., C➤pm− versus Ctl➤pm− *P* < 0.0001, as determined by log-rank test; YAP, Y➤pm+ versus Ctl➤pm+ *P* < 0.0001, Y➤pm− versus Ctl➤pm− *P* < 0.0001, as determined by log-rank test; PLCβ4, PLC➤pm+ versus Ctl➤pm+ n.s., PLC➤pm− versus Ctl➤pm− *P* < 0.0001, as determined by log-rank test. (D) Kaplan–Meier curves show that YAP cooperates with *mitfa*$^{-/-}$ in a *tp53*-WT background. Overall survival of Y➤m+ versus YAP➤m−, significant to *P* < 0.0001, as determined by log-rank test. (E) Kaplan–Meier curves of Q➤Bpm− versus Bpm− controls, with Q➤pm− from *B* shown for comparison, show that *GNAQ*^{Q209L} is dominant over *BRAF*^{V600E} in allowing tumors to form the *mitfa*$^{-/-}$ background. Statistical significance of overall survival is *P* < 0.0001 for Q➤Bpm− versus Bpm− and *P* = 0.0003 for Q➤Bpm− versus Q➤pm−, as determined by log-rank test.

context, the overall survival of C➤pm+ zebrafish was similar to that of Ctl➤pm+ controls (Fig. 3 *C, Top Left*). Despite these kinetics, at the time of death, approximately half of the C➤pm+ zebrafish carried UM that were frequently pigmented, while the remainder had only GFP$^−$ MPNSTs due to the

genome-wide presence of the *tp53*$^{-/-}$ alleles (Fig. 3 *C, Top Left*). Thus, we conclude that CYSLTR2^{L129Q} is sufficient to promote UM in cooperation with *tp53*$^{-/-}$. We then examined the C➤pm− zebrafish and found that their lifespan was much shorter than the C➤pm+ counterparts and that now 100% of these animals developed UM (Fig. 3 *C, Top Right*). Thus *mitfa*$^{-/-}$ also cooperates with CYSLTR2^{L129Q}-driven tumorigenesis, mirroring our *mitfa*$^{-/-}$ results with oncogenic GNAQ.

Next, we wanted to test the relative contributions of GNAQ's downstream signaling axes, YAP and PLCβ. YAP is not mutated in patient samples. Thus, to test its role, we used an engineered mutant YAP$^{S127A; S381A}$ (YAP^{AA}, abbreviated "Y") which is constitutively nuclear and thus active (45). We injected YAP^{AA} into *tp53*$^{-/-}$ and *tp53*$^{-/-}$;*mitfa*$^{-/-}$ zebrafish embryos (Y➤pm+ and Y➤pm−) and found that this activated form of YAP drove extremely rapid UM in both contexts, yielding tumors with similar kinetics regardless of *mitfa* status (Fig. 3 *C, Middle*). Given this potent tumorigenicity and our finding that *mitfa*$^{-/-}$ reduces reliance on *tp53*$^{-/-}$ mutation with oncogenic GNAQ, we also injected mutant active YAP into either WT or *mitfa*$^{-/-}$ embryos. The resulting Y➤m− formed UM tumors with high penetrance (59%), whereas Y➤m+ zebrafish developed UM tumors at very low penetrance and long latency (Fig. 3*D*). Thus, similar to its role in GNAQ-driven tumorigenesis, *mitfa* is a bona fide tumor suppressor in YAP^{AA}-driven UM.

Mutation of the PLCβ isoform PLCβ4 at amino acid D630 is observed in ~20 to 30% of GNAQ/11-WT human UM tumors (17) and has been shown to increase PLCβ4 signaling (18), but the oncogenic potential of this mutation has not been investigated in an autochthonous in vivo tumor model. To determine whether the PLCβ arm of GNAQ can substitute for GNAQ in driving tumorigenesis, we mosaically expressed the patient-associated PLCβ4^{D630Y} (abbreviated "PLC") mutation in both *tp53*$^{-/-}$ and *tp53*$^{-/-}$;*mitfa*$^{-/-}$ zebrafish. Survival of PLC➤pm+ zebrafish was similar to that of Ctl➤pm+ controls (Fig. 3 *C, Bottom Left*), and only extremely rarely did a PLC➤pm+ zebrafish develop UM before succumbing to the MPNST phenotype of the *tp53* mutants. In contrast, PLC➤pm− had a shorter lifespan than Ctl➤pm− controls, and 68% developed UM (Fig. 3 *C, Bottom Right*). Thus, the *mitfa*$^{-/-}$ context enables PLCβ4^{D630Y} to yield tumors in the melanocyte lineage, in stark contrast to the *mitfa*-WT background. We have probed the tumors in all aforementioned genotypes for YAP and ERK activation and will address these results below.

GNAQ^{Q209L} Can Overcome the Tumorigenic Block in Tg(mitfa:BRAF^{V600E});tp53$^{-/-}$;mitfa$^{-/-}$. Our data highlight two distinct differences between UM and CM. First, the *mitfa*$^{-/-}$ context promotes the tumorgenicity of the UM-driving *GNAQ* mutation but is completely incompatible with BRAF^{V600E}-driven tumorigenesis associated with CM. Second, although these oncogenes can both induce MEK/ERK as a downstream effector, phospho-ERK is key for CM but is down-regulated in *mitfa*$^{-/-}$ UM. Given these findings, we wanted to coexpress oncogenic *GNAQ* and *BRAF* in a *tp53*$^{-/-}$;*mitfa*$^{-/-}$ background to determine which would be dominant, the protumorigenic phenotype or the antitumorigenic phenotype of *mitfa*$^{-/-}$ in the context of *GNAQ*^{Q209L} and *BRAF*^{V600E}, respectively. We used the GFP–GOI system to express GNAQ^{Q209L} in the melanocytes of *Tg(mitfa:BRAF^{V600E}); tp53*$^{-/-}$;*mitfa*$^{-/-}$ zebrafish (Q➤Bpm−) to determine whether the protumorigenic phenotype of *mitfa*$^{-/-}$ in the context of *GNAQ*^{Q209L} was

dominant over its antitumorigenic phenotype in the context of *BRAF^{V600E}*. Strikingly, we found that Q→Bpm− rapidly formed tumors, demonstrating that GNAQ^{Q209L} can overcome the tumorigenic block in Bpm− (Fig. 3E).

CYSLTR2^{L129Q}-, YAP^{AA}-, and PLCβ4^{D630Y}-Driven Tumors Are Deficient for Hyperactive ERK Staining in the mitfa^{−/−} Context. We next studied the tumor phenotypes of CYSLTR2^{L129Q}-, YAP^{AA}-, or PLCβ4^{D630Y}-driven UM. As noted above, Qpm+ and Qpm− tumors display histopathological differences, and they were mirrored in CYSLTR2^{L129Q}-, YAP^{AA}-, or PLCβ4^{D630Y}-driven UM. Thus, *mitfa* deficiency has a profound impact on UM regardless of the specific driver (Fig. 4A). We then performed IHC on CYSLTR2^{L129Q}-, YAP^{AA}-, or PLCβ4^{D630Y}-driven UM to determine YAP and ERK activation as shown by nuclear YAP and phosphorylated ERK, respectively. CYSLTR2^{L129Q} is predicted to drive UM formation through activation of GNAQ, and, accordingly, the staining mirrored that of GNAQ^{Q209L}-driven tumors. Specifically, in the *mitfa*-WT context, the C→pm+ UM displayed both strong staining for YAP+ nuclei and phospho-ERK, while C→pm− UM had a similar level of YAP+ nuclei but a near-complete absence of phospho-ERK staining (Fig. 4 A and C). This reinforces the similarities between GNAQ^{Q209L}- and CYSLTR2^{L129Q}-driven tumors and supports the notion that CYSLTR2 drives in vivo tumorigenesis through GNAQ activation. Y→pm+ and Y→pm− UM had very high levels of nuclear YAP, as expected, and they also largely lacked phosphorylated ERK, consistent with the idea that activated YAP is not known to cross-talk to the MEK/ERK signaling cascade (Fig. 4 A and C). This again highlights a key role for YAP in UM.

We next examined the tumors that arose in PLC→pm− zebrafish. Remarkably, these tumors displayed near-complete absence of phospho-ERK activation (Fig. 4 A and C). This was surprising, as it raised the question of how PLCβ4 acts to induce tumors if not through ERK signaling. In likely answer to this question, we found that the PLC→pm− tumors also displayed strong nuclear YAP staining (Fig. 4A). This was completely unexpected, as the PLCβ and YAP pathways are thought to be distinct. Interestingly, we did obtain a single PLCβ4-driven UM in the *p53^{−/−};mitfa^{+/+}* background. This tumor also displayed strong nuclear YAP/TAZ but additionally showed widespread phospho-ERK activation, establishing that PLCβ4^{D630Y} does activate the MAPK pathway in the presence of WT *mitfa* (*SI Appendix*, Fig. S12). Taken together, our data support two key conclusions. First, activated YAP is sufficient to drive UM, while hyperactive ERK seems to be deemphasized and potentially dispensable. Second, MITF deficiency acts to promote UM, and it consistently suppresses ERK signaling, regardless of the oncogenic driver, while maintaining YAP signaling. This reinforces the notion that active YAP is a central feature of UM.

Finally, we examined the signaling pathways that were active in the Q→Bpm− tumors. These tumors also displayed nuclear YAP and were negative for phospho-ERK, despite expressing oncogenic BRAF (Fig. 4 B and C). These findings argue that the *mitfa^{−/−}* cell state somehow acts to suppress ERK activation, even in the presence of *BRAF^{V600E}*. We believe that this finding offers a clear explanation why oncogenic BRAF is unable to drive tumor formation in the absence of *mitfa*; this genetic background down-regulates the MEK/ERK signaling that is required for oncogenic *BRAF* to drive melanoma. It is
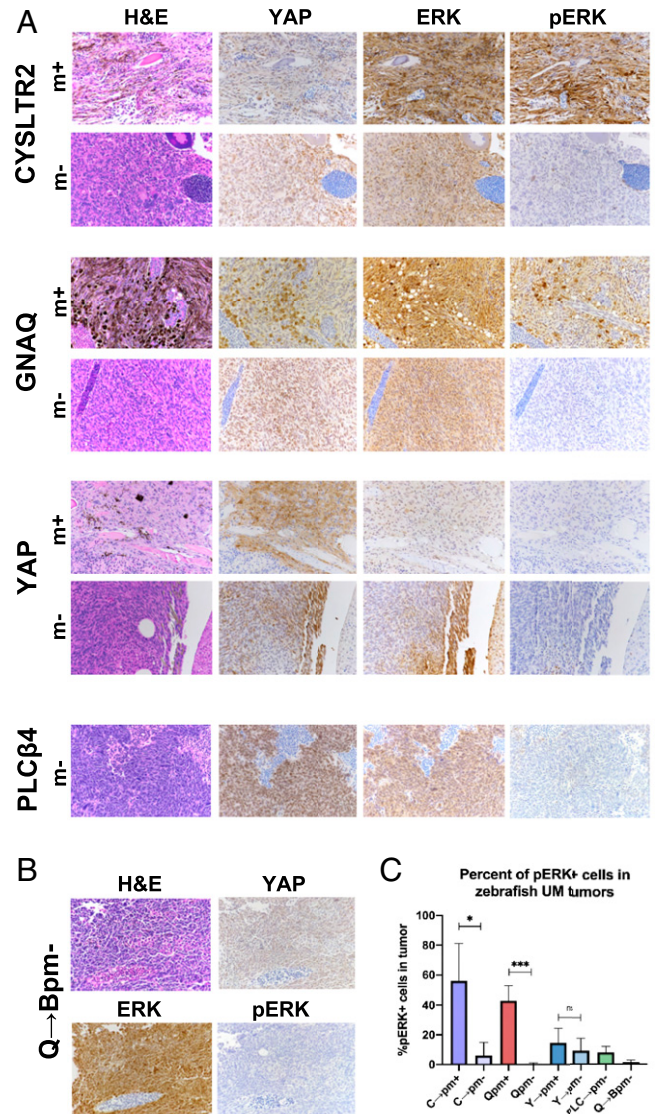
Fig. 4. CYSLTR2^{L129Q}-, YAP^{AA}-, and PLCβ4^{D630Y}-driven tumors do not display hyperactive ERK staining in the *mitfa^{−/−}* context. Genotype abbreviations are as described in Fig. 3. (A and B) Representative images of H&E staining and IHC for YAP, ERK, or phospho-ERK (pERK) on the indicated tumor genotypes. YAP activation is determined by nuclear localization and ERK activation by phospho-ERK. (A) C→pm+ tumors and Qpm+ tumors are positive for nuclear YAP and phospho-ERK, while C→pm−, Qpm−, and PLC→pm− tumors display only YAP activation; n ≥ 3 for all genotypes, except n = 2 for each Y→pm− and C→pm+ IHC stains. (B) Q→Bpm− displays nuclear YAP but not phospho-ERK; n = 5 for all stains. (C) Graph shows the percent of UM tumor cells positive for phospho-ERK quantified by QuPath (n ≥ 3 for all genotypes, except n = 2 for Y→pm− and C→pm+), and error bars denote SD. Statistical significance is as follows: C→pm+ versus C→pm− P = 0.0435, Q→pm+ versus Q→pm− P = 0.0001, Y→pm+ versus Y→pm− P = 0.551, as determined by Student's unpaired t test.

also consistent with our hypothesis that hyperactive ERK may be dispensable for GNAQ^{Q209L}-driven UM tumors.

Decreased Expression of MITF Target Genes and a MAPK Transcriptional Program Correlate with Poor UM Patient Survival. Overall, we have demonstrated that *mitfa* deficiency accelerates tumorigenesis, regardless of UM oncogenic driver, and the resulting tumors show significant down-regulation of hyperactive ERK in our zebrafish model. To translate our findings to human UM, we analyzed the PanCancer UM cohort (n = 80 patients) in The Cancer Genome Atlas (TCGA) to determine the role of MITF and MAPK signaling in UM.
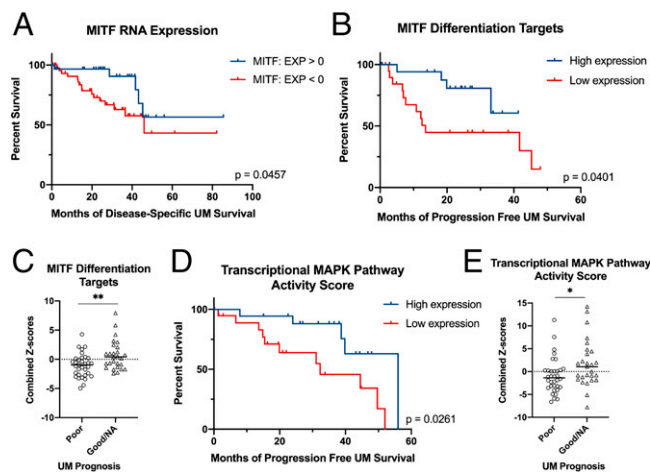
Fig. 5. Decreased expression of MITF target genes and decreased MAPK transcriptional activity correlate with poor UM patient survival. RNA sequencing of primary human UM ($n = 80$ patients) and the corresponding survival data were obtained from TCGA PanCancer Atlas database. (A) Patients with relatively lower MITF RNA expression (z score < 0; $n = 49$) have significantly decreased ($P = 0.0457$, determined by log-rank test) disease-free survival compared to patients with relatively higher MITF RNA expression (z score > 0; $n = 31$). (B) Z scores for the MITF differentiation target genes DCT, TYR, TYRP1, and SILV were calculated and summed for each UM tumor, and patients in the lower quartile ($n = 20$) were found to have significantly decreased ($P = 0.04$, determined by log-rank test) progression-free survival compared to patients in the upper quartile ($n = 20$). (C) UM patients were binned by "poor prognosis" (those deceased or with progression of the disease [$n = 34$]) versus "good/NA prognosis" (those last reported as living without progression for at least 2 y [$n = 27$]). The poor prognosis cohort showed significantly lower combined z scores for the four MITF differentiation targets ($P = 0.0041$, determined by Student's unpaired t test; line denotes median). (D) Z scores for genes in the transcriptional MAPK activity gene set were calculated and summed. Patients in the lower quartile ($n = 20$) showed significantly decreased ($P = 0.0261$, determined by log-rank test) progression-free survival compared to patients in the upper quartile ($n = 20$). (E) UM patients with poor prognosis (binned as described in C) have a significantly lower transcriptional MAPK pathway activity combined z scores ($P = 0.0218$, determined by Student's unpaired t test; line denotes median) than the good/NA prognosis cohort.

Consistent with our zebrafish findings, we have found that relatively lower MITF RNA levels correlated with decreased disease-specific UM survival (Fig. 5A). As MITF activity is heavily regulated at a posttranslational level (46), we examined MITF target gene expression as a readout for MITF activity. For this, we considered four key MITF differentiation targets, DCT, TYR, TYRP1, and SILV, which were also significantly down-regulated in our zebrafish Qpm− compared to Qpm+ RNA-sequencing data. We calculated and summed their z scores to yield a combined z score for MITF differentiation targets for each UM patient. Notably, low expression (lower quartile, $n = 20$ patients) significantly correlated with decreased progression-free UM survival compared to high expression (top quartile, $n = 20$ patients), arguing that decreased MITF activity correlates with poor survival (Fig. 5B). As an alternative approach, we binned the UM patients into "poor" prognosis, including patients that are deceased or had progression of the disease, and "good/NA" prognosis, including patients that are last reported living without progression for at least 2 y. Importantly, the UM patients with poor prognosis had significantly lower combined MITF differentiation target z scores (Fig. 5C).

Finally, given that loss of MAPK activity correlates strongly with accelerated UM tumorigenesis in our zebrafish model, we sought to determine if MAPK activity correlated with poor survival or prognosis in UM. Thus, we calculated and summed the z scores for the transcriptional MAPK pathway activity

genes (43) for each UM patient. Consistent with our zebrafish model, low MAPK activity expression (lower quartile, $n = 20$ patients) significantly correlated with decreased progression-free UM survival compared to high expression (top quartile, $n = 20$ patients; Fig. 5D). Moreover, when UM patients were binned by prognosis, as described above, the poor prognosis cohort had a significantly lower combined transcriptional MAPK activity z score (Fig. 5E). Overall, our analyses of UM TCGA patient data are consistent with the role of low MITF and decreased MAPK activity in promoting UM in zebrafish.

Discussion

This study examined the importance of different GNAQ effector pathways and also established the role of MITF in UM in vivo. Our results from these two analyses, some of which are included in the Ph.D. dissertation by Hagen (47), intersect remarkably well to reveal the key signaling events in UM and the fundamental differences between UM and CM.

Two major GNAQ effector pathways have been implicated in UM: PLCβ4–PKC–ERK (11, 12) and nuclear YAP (13–15). We show that patient-derived mutations $GNAQ/11^{Q209L}$, or the rarer $CYSLTR2^{L129Q}$, drive UM tumors that display both ERK and YAP activation in the presence of WT *mitfa* and mutant *tp53*. Thus, at least in this WT *mitfa* and mutant *tp53* context, either or both of these signaling pathways could be enabling tumorigenesis. However, our additional findings provide compelling evidence that YAP signaling is the critical driver, and hyperactive ERK may be dispensable for UM. First, activated YAP is clearly sufficient to cooperate with mutant *tp53* to drive UM, and these tumors lack phospho-ERK signal. Second, the patient-derived PLCβ4 mutation $PLCβ4^{D630Y}$ almost never drove tumorigenesis in the context of WT *mitfa* and mutant *tp53*, despite its ability to activate the ERK pathway. Moreover, the one tumor we were able to examine showed YAP/TAZ activation. Finally, when combined with *mitfa* loss, $GNAQ/11^{Q209L}$, $CYSLTR2^{L129Q}$, activated YAP, and $PLCβ4^{D630Y}$ all yielded tumors that have high levels of nuclear YAP and down-regulated phospho-ERK. We had not anticipated that $PLCβ4^{D630Y}$ could activate YAP, but there is precedent for this in other tumor types. For example, YAP activation has been reported in both $HRAS^{V12}$-driven zebrafish malignant brain tumors (48) and activated PI3K-driven mammary tumorigenesis (49).

Data from prior studies is entirely consistent with our hypothesis that phospho-ERK may be dispensable for $GNAQ^{Q209L}$-driven UM. Low and sporadic phospho-ERK staining, in concert with high nuclear YAP, was reported in a zebrafish $Tg(mitfa:GNAQ^{Q209P});tp53^{-/-}$ UM model (50). More importantly, variable phospho-ERK staining has clearly been observed in primary UM patient samples (51–54). Accordingly, a MEK inhibitor did not affect UM tumor growth in transplanted mice in vivo (12), and MEK/ERK inhibitors have proven ineffective in UM clinical trials (20), in stark contrast to their success in treating CM.

Our data also reveal a tumor-suppressive role for MITF in UM. This further underscores the differences between UM and CM. It is well established that MITF is required for both development and maintenance of CM (34, 37). In contrast, there were limited prior data on MITF's role in UM. Indeed, the existing studies make conflicting conclusions, with one showing that low MITF correlates with more invasive, aggressive epithelioid UM tumors (55) and another concluding that MITF level

has no bearing on cell characteristics or patient survival in UM (56). Notably, MITF resides on chromosome 3, and monosomy 3 is the best indicator for metastatic disease in UM (57). Our study is the first to modulate MITF expression in an in vivo autochthonous UM model. This showed that *mitfa* loss promotes both the onset and the aggressiveness of *Tg(mitfa: GNAQ/11^{Q209L});tp53$^{-/-}$* UM tumors. Moreover, *mitfa* deficiency is sufficient to cooperate with oncogenic GNAQ/11 to drive *tp53*-WT UM. Thus, *mitfa* functions as a bona fide tumor suppressor in UM, in direct opposition to its role in CM. Interestingly, our data also offer a simple explanation why MITF deficiency is incompatible with CM: MITF loss appears to down-regulate MEK/ERK signaling, which BRAF/NRAS rely on to drive CM tumorigenesis.

One limitation of our zebrafish model is that *tp53* mutation is required for UM tumor formation (except when combined with *mitfa* deficiency). Although CDKN2A promoter methylation and MDM2 overexpression arise in some human UM (58), *tp53* is rarely mutated itself. Instead, a significant fraction of UM displays BAP1 loss, which has been linked to metastasis and poor survival (59). Sadly, there has been little success in mirroring the consequences of BAP1 loss in UM model organisms. BAP1 loss did decrease the survival of a GNA11^{Q209L} mouse model but does so by driving aggressive skin melanoma, not metastasis of UM (12). We generated a zebrafish BAP1-null allele using CRISPR, but this did not enable GNAQ^{Q209L}-driven tumorigenesis. The difficulty in generating an animal model that recapitulates the role of BAP1 in human UM has yet to be explained but could be because BAP1 is a deubiquitinase and may have different functional targets in different organisms. Still, there is a great need for a faithful UM model of BAP1.

Despite these modeling issues, we speculate that *mitfa* deficiency in our zebrafish model may be acting in an analogous manner to BAP1 loss. Specifically, deletion of BAP1 in UM cell lines was shown to promote their dedifferentiation (60). *mitfa* deficiency prevents melanocyte differentiation and allows undifferentiated melanocyte precursor cells, which do not exist in normal adult zebrafish, to persist in adult *mitfa$^{-/-}$* zebrafish. It is possible that *mitfa* loss could simply increase the number and persistence of the cell of origin for UM. This could explain the higher rate of initiation and thus the accelerated onset of our zebrafish *mitfa$^{-/-}$* UM, but it is unclear how this would account for their increased aggressiveness. Thus, either alternatively or in addition to this increased target cell hypothesis, we favor the notion that the differentiation block of the *mitfa$^{-/-}$* melanocyte lineage cells may lock them into a different progenitor state that promotes tumorigenesis and invasive phenotypes.

Our data clearly establish that this *mitfa$^{-/-}$* state dramatically alters oncogenic signaling. First, it clearly suppresses GNAQ/11^{Q209L}-driven PLCβ4–PKC pathway activation, as evidenced by decreases in MAPK, Akt, and NF-κB activation. Second, several lines of evidence suggest activation of the MYC transcription factor in GNAQ^{Q209L}; *mitfa$^{-/-}$* tumors. MYC promotes cell cycle entry, DNA repair, translation, and chromatin reorganization (61)—all processes that are enriched in our Qpm− tumors. Moreover, our RNA-sequencing and proteomics data showed that Qpm− tumors have higher levels of mycb mRNA (the zebrafish MYC ortholog) and increased levels or activation of key proteins that have been previously linked to MYC activation, including NPM1 (62), WDR5 (63), and CDK7 (44). Notably, in part through CDK7 activation, MITF deficiency in melanoma has been shown to activate

c-MYC, which can substitute for MITF's role in transcription initiation but not melanocyte differentiation (44). More importantly, 73.8% of human UM cases display MYC copy number gains, and higher copy number correlates with more aggressive tumors and poor patient survival (64). Given these findings, we speculate that the *mitfa$^{-/-}$* state acts to accelerate GNAQ^{Q209L} progression in part through MYC activation.

The identified tumor-suppressive role for MITF in our zebrafish UM model also fits with previously unexplained observations in a GNAQ^{Q209L} UM mouse model (65). In this model, GNAQ^{Q209L} is activated by MITF-Cre, and the mice develop tumors exceptionally quickly without any cooperating mutations. This is in stark contrast to both human UM tumor samples (66) and other GNAQ/11^{Q209L} mouse models (12, 14, 66) in which aggressive tumorigenesis requires cooperating mutations. Interestingly, the MITF-Cre knock-in allele used for the discordant GNAQ^{Q209L} UM mouse model is known to cause microphthalmia (65), a hallmark of MITF hypomorphs. Notably, when tyrosinase-Cre is used instead of MITF-Cre, activated GNAQ/11^{Q209L} only drives aggressive tumorigenesis in the presence of a cooperating mutation (12, 65). Before our studies, the favored explanation for these findings was the difference in developmental timing of MITF-Cre versus tyrosinase-Cre. Our data do not rule out this model. However, having shown that MITF is a tumor suppressor in UM, we hypothesize that hypomorphic MITF in the *GNAQ^{Q209L}; MITF-Cre* mouse model serves as a cooperating mutation to enable rapid tumorigenesis. If true, this shows that the role of MITF in UM is conserved between zebrafish and mice.

Together, our findings outline a tumor-suppressive role for MITF in UM, demonstrate that hyperactive ERK may be dispensable for UM tumorigenesis, and show that YAP is sufficient to drive UM and is active in all GNAQ/11 pathway–driven tumors. These results have significant implications for human disease. Therapeutic targeting of MITF has been widely proposed as a potential therapy for CM and by extension has also been speculated as a treatment for UM. Our results suggest that MITF inhibition should not be attempted in UM as it would likely be detrimental to patients, barring the possibility that MITF inhibition in established tumors has a different outcome than in developing tumors. Finally, our results have the potential to explain the clinical ineffectiveness of PKC/MEK/ERK inhibitors for UM and argue strongly that targeting YAP or MYC is a more promising therapeutic strategy.

Materials and Methods

Zebrafish Lines. Zebrafish were maintained according to protocols approved by the Committee on Animal Care at Massachusetts Institute of Technology (MIT). Experiments were performed in the AB/Tübingen (TAB5/14) genetic background and the *mitfa$^{w2/w2}$* background, which was derived by breeding the *roy* mutation out of casper zebrafish. *Tg(mitfa:GNAQ^{Q209L});tp53$^{-/-}$* zebrafish are the Q-1 transgenic line from Perez et al. (40). Zebrafish were killed upon moribund tumor burden for Kaplan-Meier curves.

Mosaic Model System. For the mosaic model, we modified the MiniCoopR vector (42) to create the GOI-GFP vector by replacing the *mitfa* coding sequence with GFP and adding a second *mitfa* promoter antiparallel to the first, which contained an EcoRI cloning entry site immediately downstream and an SV40 termination sequence. Gibson assembly was used to insert *GNAQ^{Q209L}* (from a Gateway vector including the *GNAQ^{Q209L}* cDNA sequence from GNA0Q000C0), *CYSLTR2^{L129Q}* (transferring CYSLTR2 from Tango-CYSLTR2 [Addgene] and creating the L129Q point mutation by site-directed mutagenesis) or *PLCB4^{D630Y}* (PCR amplifying *PLCB4* from HEK293 cDNA, confirming by sequencing, and creating

the D630Y mutation by site-directed mutagenesis), and YAP^{S127A,S381A} (from murine stem cell virus MSCV-YAP^{S127A,S381A}, provided by R. Hynes, MIT). GOI–GFP vectors (50 ng/μL) and Tol2 transposase mRNA (50 ng/μL) were coinjected into single-cell zebrafish embryos using a microinjector. Embryos were screened for GFP expression at 5 d after fertilization, and GFP$^+$ embryos were raised to adulthood and monitored for tumors as above.

Tumor Burden, *tp53* Analysis, and IHC. Tumor burden quantification and analysis of *tp53* LOH are described in *SI Appendix, Supplemental Materials and Methods*. IHC analyses and imaging were performed as previously described (40). The following were the primary antibodies used: YAP (1:200; 4912, Cell Signaling), ERK1/2 (1:200; 4696, Cell Signaling), phospho-ERK1/2 (1:200; 4370, Cell Signaling), phospho-Akt (1:50; 4060, Cell Signaling), pan-Akt (1:200; 4691, Cell Signaling), NF-κB p65/RelA (1:200; 8242, Cell Signaling), phospho-MEK1/2 (1:50; 2338, Cell Signaling), and YAP/TAZ (1:200; 8418, Cell Signaling). IHC quantification was performed as described in *SI Appendix, Supplemental Materials and Methods*.

RNA Sequencing. Zebrafish tumors were excised, and RNA was purified by using TRIzol extraction. RNA sequencing was conducted as described in *SI Appendix, Supplemental Materials and Methods*. A PCA was performed with R version 4.0.3 using plotPCA on the top 500 variable genes from DESeq2 version 1.30.1. Combined *z* scores were calculated for specific gene lists (24, 43) (Dataset S1) by calculating the *z* score for each zebrafish gene across each of the RNA-sequencing samples and summing the *z* scores for each gene in the gene list for each sample. The RNA-sequencing data have been deposited in the Gene Expression Omnibus under accession code GSE190802.

qRT-PCR. Zebrafish tumor RNA was reverse transcribed using SuperScript III reverse transcriptase (Thermo Fisher). Real-time PCR reactions were performed using FAST-SYBR Green on a StepOnePlus real-time PCR system (Applied Biosystems). Data were analyzed using the $\Delta\Delta C_T$ method, and relative mRNA levels were normalized to *actb2* (β-actin 2) levels. The following were the primers used: *actb2* forward 5′-GCCAACAGGGAAAAGATGACAC-3′, *actb2* reverse 5′-GTAC GACCGGAGGCATACAG; *dusp4* forward 5′-CCATAAAGAGGACATCAGCTC-3′ and *dusp4* reverse 5′-AGCACCTGAGACTCGAACTG-3′; *dusp6* forward 5′-GAATGAAGG ACGAGGGCTAC-3′ and *dusp6* reverse 5′-GGAGTCAGAGCTGATTCTGAG-3′.

Proteomics. Zebrafish with large external tumors were killed in ice water, and the tumors were excised, flash-frozen in liquid nitrogen, and homogenized using a GenoGrinder. These samples were resuspended in protein lysis buffer (150 mM NaCl, 50 mM Tris-HCl pH 7.5, 0.5% Nonidet P-40, 5 mM β-mercaptoethanol, 1× ethylenediaminetetraacetic acid [EDTA]-free protease

inhibitor cocktail [Roche, COEDTAF-RO], and 1× PhosSTOP [Roche, PHOSS-RO]) and lysed for 10 min on ice with intermittent vortexing. The debris was pelleted, and the supernatant was quantified using a Bradford assay. Protein (0.5 to 1 mg) from each sample was used for proteomics analyses (*n* = 5 per genotype). Total peptide and phospho-peptide sample preparation, liquid chromatography-tandem mass spectrometry, and GSEA methods and visualization are described in *SI Appendix, Supplemental Materials and Methods*. The mass spectrometry proteomics data have been deposited to the ProteomeXchange Consortium via the PRIDE (67) partner repository with the dataset identifier PXD030527 and 10. 6019/PXD030527. Processed phospho-proteomics and total proteomics data can be found in Datasets S2 and S3, respectively.

Patient Data (TCGA) Analysis. RNA sequencing of primary tumors and corresponding survival data were obtained from TCGA PanCancer Atlas database of UM (*n* = 80 patients). *Z* scores were calculated for each queried gene across each patient in the "mRNA expression, RSEM, batch normalized from the Illumina HiSeq_RNAseqV2 RNA-sequencing" dataset.

Statistical Analysis. Prism software was used to analyze data, draw graphs, and perform statistical analyses. Log-rank tests were used for zebrafish and human patient Kaplan–Meier/survival curves. All other statistical analyses were performed using Student's unpaired *t* tests. Data are presented as mean ± SD (error bars). For statistical significance, *$P \leq 0.05$, **$P \leq 0.01$, ***$P \leq 0.001$, and ****$P \leq 0.0001$ were considered significant; n.s. refers to not significant ($P > 0.05$).

Data Availability. RNA-sequencing data have been deposited in the Gene Expression Omnibus under accession no. GSE190802 (68). Proteomics data have been deposited in the ProteomeXchange Consortium via the PRIDE partner repository under accession no. PXD030527 (69). All other study data are included in the article and/or supporting information.

1. B. A. Krantz, N. Dave, K. M. Komatsubara, B. P. Marr, R. D. Carvajal, Uveal melanoma: Epidemiology, etiology, and treatment of primary disease. *Clin. Ophthalmol.* **11**, 279–289 (2017).
2. R. D. Carvajal *et al.*, Metastatic disease from uveal melanoma: Treatment options and future prospects. *Br. J. Ophthalmol.* **101**, 38–44 (2017).
3. J. Yang, D. K. Manson, B. P. Marr, R. D. Carvajal, Treatment of uveal melanoma: Where are we now? *Ther. Adv. Med. Oncol.* **10**, 1758834018757175 (2018).
4. W. H. Ward, J. M. Farma, Eds., *Cutaneous Melanoma: Etiology and Therapy* (Codon Publications, 2017).
5. G. C. Leonardi *et al.*, Cutaneous melanoma: From pathogenesis to therapy (Review). *Int. J. Oncol.* **52**, 1071–1080 (2018).
6. F. G. Haluska, F. S. Hodi, Molecular genetics of familial cutaneous melanoma. *J. Clin. Oncol.* **16**, 670–682 (1998).
7. H. Davies *et al.*, Mutations of the BRAF gene in human cancer. *Nature* **417**, 949–954 (2002).
8. C. D. Van Raamsdonk *et al.*, Mutations in GNA11 in uveal melanoma. *N. Engl. J. Med.* **363**, 2191–2199 (2010).
9. C. D. Van Raamsdonk *et al.*, Frequent somatic mutations of GNAQ in uveal melanoma and blue naevi. *Nature* **457**, 599–602 (2009).
10. A. R. Moore *et al.*, Recurrent activating mutations of G-protein-coupled receptor CYSLTR2 in uveal melanoma. *Nat. Genet.* **48**, 675–680 (2016).
11. X. Chen *et al.*, RasGRP3 mediates MAPK pathway activation in GNAQ mutant uveal melanoma. *Cancer Cell* **31**, 685–696.e6 (2017).
12. A. R. Moore *et al.*, GNA11 Q209L mouse model reveals RasGRP3 as an essential signaling node in uveal melanoma. *Cell Rep.* **22**, 2455–2468 (2018).
13. F.-X. Yu *et al.*, Mutant Gq/11 promote uveal melanoma tumorigenesis by activating YAP. *Cancer Cell* **25**, 822–830 (2014).
14. X. Feng *et al.*, Hippo-independent activation of YAP by the GNAQ uveal melanoma oncogene through a trio-regulated rho GTPase signaling circuitry. *Cancer Cell* **25**, 831–845 (2014).
15. X. Feng *et al.*, A platform of synthetic lethal gene interaction networks reveals that the GNAQ uveal melanoma oncogene controls the Hippo pathway through FAK. *Cancer Cell* **35**, 457–472 (2019).
16. F. Zanconato, M. Cordenonsi, S. Piccolo, YAP/TAZ at the roots of cancer. *Cancer Cell* **29**, 783–803 (2016).
17. P. Johansson *et al.*, Deep sequencing of uveal melanoma identifies a recurrent mutation in PLCB4. *Oncotarget* **7**, 4624–4631 (2016).
18. H. T. N. Phan, N. H. Kim, W. Wei, G. G. Tall, A. V. Smrcka, Uveal melanoma-associated mutations in PLCβ4 are constitutively activating and promote melanocyte proliferation and tumorigenesis. *Sci. Signal.* **14**, eabj4243 (2021).
19. T. Steeb, A. Wessely, T. Ruzicka, M. V. Heppt, C. Berking, How to MEK the best of uveal melanoma: A systematic review on the efficacy and safety of MEK inhibitors in metastatic or unresectable uveal melanoma. *Eur. J. Cancer* **103**, 41–51 (2018).
20. M. J. Jager *et al.*, Uveal melanoma. *Nat. Rev. Dis. Primers* **6**, 24 (2020).
21. H. Li *et al.*, YAP/TAZ activation drives uveal melanoma initiation and progression. *Cell Rep.* **29**, 3200–3211 (2019).
22. Y. J. Kim *et al.*, YAP activity is not associated with survival of uveal melanoma patients and cell lines. *Sci. Rep.* **10**, 6209 (2020).
23. G. Prescher *et al.*, Prognostic implications of monosomy 3 in uveal melanoma. *Lancet* **347**, 1222–1225 (1996).
24. Y. Cheli, M. Ohanna, R. Ballotti, C. Bertolotto, Fifteen-year quest for microphthalmia-associated transcription factor target genes. *Pigment Cell Melanoma Res.* **23**, 27–40 (2010).
25. R. L. Mort, I. J. Jackson, E. E. Patton, The melanocyte lineage in development and disease. *Development* **142**, 620–632 (2015).
26. M. L. Hartman, M. Czyz, Pro-survival role of MITF in melanoma. *J. Invest. Dermatol.* **135**, 352–358 (2015).
27. J. Vachtenheim, The many roles of MITF in melanoma. *Single Cell Biol.* **6**, 1000162 (2017).
28. S. Carreira *et al.*, Mitf regulation of dia1 controls melanoma proliferation and invasiveness. *Genes Dev.* **20**, 3426–3439 (2006).
29. K. S. Hoek *et al.*, In vivo switching of human melanoma cells between proliferative and invasive states. *Cancer Res.* **68**, 650–656 (2008).
30. Y. Cheli *et al.*, Mitf is the key molecular switch between mouse or human melanoma initiating cells and their differentiated progeny. *Oncogene* **30**, 2307–2318 (2011).
31. N. K. Haass *et al.*, Real-time cell cycle imaging during melanoma growth, invasion, and drug response. *Pigment Cell Melanoma Res.* **27**, 764–776 (2014).
32. S. Aida *et al.*, MITF suppression improves the sensitivity of melanoma cells to a BRAF inhibitor. *Cancer Lett.* **409**, 116–124 (2017).
33. J. Müller *et al.*, Low MITF/AXL ratio predicts early resistance to multiple targeted drugs in melanoma. *Nat. Commun.* **5**, 5712 (2014).

34. J. A. Lister *et al.*, A conditional zebrafish MITF mutation reveals MITF levels are critical for melanoma promotion vs. regression in vivo. *J. Invest. Dermatol.* **134**, 133–140 (2014).

35. R. E. Bell, C. Levy, The three M's: Melanoma, microphthalmia-associated transcription factor and microRNA. *Pigment Cell Melanoma Res.* **24**, 1088–1106 (2011).

36. M. R. Eccles *et al.*, MITF and PAX3 play distinct roles in melanoma cell migration: Outline of a "genetic switch" theory involving MITF and PAX3 in proliferative and invasive phenotypes of melanoma. *Front. Oncol.* **3**, 229 (2013).

37. T. Strub *et al.*, Essential role of microphthalmia transcription factor for DNA replication, mitosis and genomic stability in melanoma. *Oncogene* **30**, 2319–2332 (2011).

38. E. E. Patton *et al.*, BRAF mutations are sufficient to promote nevi formation and cooperate with p53 in the genesis of melanoma. *Curr. Biol.* **15**, 249–254 (2005).

39. R. White, K. Rose, L. Zon, Zebrafish cancer: The state of the art and the path forward. *Nat. Rev. Cancer* **13**, 624–636 (2013).

40. D. E. Perez, A. M. Henle, A. Amsterdam, H. R. Hagen, J. A. Lees, Uveal melanoma driver mutations in GNAQ/11 yield numerous changes in melanocyte biology. *Pigment Cell Melanoma Res.* **31**, 604–613 (2018).

41. J. A. Lister, C. P. Robertson, T. Lepage, S. L. Johnson, D. W. Raible, nacre encodes a zebrafish microphthalmia-related protein that regulates neural-crest-derived pigment cell fate. *Development* **126**, 3757–3767 (1999).

42. C. J. Ceol *et al.*, The histone methyltransferase SETDB1 is recurrently amplified in melanoma and accelerates its onset. *Nature* **471**, 513–517 (2011).

43. M.-C. Wagle *et al.*, A transcriptional MAPK pathway activity score (MPAS) is a clinically relevant biomarker in multiple cancer types. *NPJ Precis. Oncol.* **2**, 7 (2018).

44. M. Seoane *et al.*, Lineage-specific control of TFIIH by MITF determines transcriptional homeostasis and DNA repair. *Oncogene* **38**, 3616–3635 (2019).

45. J. M. Lamar *et al.*, The Hippo pathway target, YAP, promotes metastasis through its TEAD-interaction domain. *Proc. Natl. Acad. Sci. U.S.A.* **109**, E2441–E2450 (2012).

46. C. R. Goding, H. Arnheiter, MITF   The first 25 years. *Genes Dev.* **33**, 983–1007 (2019).

47. H. R. Hagen, "A GNAQ/11-driven zebrafish cancer model identifies MITF and YAP as key determinants for uveal melanoma," PhD thesis, Massachusetts Institute of Technology, Cambridge, MA (2019).

48. M. Mayrhofer *et al.*, A novel brain tumour model in zebrafish reveals the role of YAP activation in MAPK- and PI3K-induced malignant growth. *Dis. Model. Mech.* **10**, 15–28 (2017).

49. Y. Zhao *et al.*, PI3K positively regulates YAP and TAZ in mammary tumorigenesis through multiple signaling pathways. *Mol. Cancer Res.* **16**, 1046–1058 (2018).

50. M. A. Mouti, C. Dee, S. E. Coupland, A. F. L. Hurlstone, Minimal contribution of ERK1/2-MAPK signalling towards the maintenance of oncogenic GNAQQ209P-driven uveal melanomas in zebrafish. *Oncotarget* **7**, 39654–39670 (2016).

51. G. Boru *et al.*, Heterogeneity in mitogen-activated protein kinase (MAPK) pathway activation in uveal melanoma with somatic GNAQ and GNA11 mutations. *Invest. Ophthalmol. Vis. Sci.* **60**, 2474–2480 (2019).

52. H. Pópulo, J. Vinagre, J. M. Lopes, P. Soares, Analysis of GNAQ mutations, proliferation and MAPK pathway activation in uveal melanomas. *Br. J. Ophthalmol.* **95**, 715–719 (2011).

53. W. Zuidervaart *et al.*, Activation of the MAPK pathway is a common event in uveal melanomas although it rarely occurs through mutation of BRAF or RAS. *Br. J. Cancer* **92**, 2032–2038 (2005).

54. A. Weber *et al.*, Absence of mutations of the BRAF gene and constitutive activation of extracellular-regulated kinase in malignant melanomas of the uvea. *Lab. Invest.* **83**, 1771–1776 (2003).

55. Y. Chen *et al.*, ZEB1 regulates multiple oncogenic components involved in uveal melanoma progression. *Sci. Rep.* **7**, 45 (2017).

56. F. Mouriaux *et al.*, Microphthalmia transcription factor analysis in posterior uveal melanomas. *Exp. Eye Res.* **76**, 653–661 (2003).

57. B. Damato *et al.*, Cytogenetics of uveal melanoma: A 7-year clinical experience. *Ophthalmology* **114**, 1925–1931 (2007).

58. S. E. Coupland, S. L. Lake, M. Zeschnigk, B. E. Damato, Molecular pathology of uveal melanoma. *Eye (Lond.)* **27**, 230–242 (2013).

59. J. W. Harbour *et al.*, Frequent mutation of BAP1 in metastasizing uveal melanomas. *Science* **330**, 1410–1413 (2010).

60. K. A. Matatall *et al.*, BAP1 deficiency causes loss of melanocytic cell identity in uveal melanoma. *BMC Cancer* **13**, 371 (2013).

61. H. Chen, H. Liu, G. Qing, Targeting oncogenic Myc as a strategy for cancer treatment. *Signal Transduct. Target. Ther.* **3**, 5 (2018).

62. Z. Li, D. Boone, S. R. Hann, Nucleophosmin interacts directly with c-Myc and controls c-Myc-induced hyperproliferation and transformation. *Proc. Natl. Acad. Sci. U.S.A.* **105**, 18794–18799 (2008).

63. L. R. Thomas *et al.*, Interaction of the oncoprotein transcription factor MYC with its chromatin cofactor WDR5 is essential for tumor maintenance. *Proc. Natl. Acad. Sci. U.S.A.* **116**, 25260–25268 (2019).

64. Y. J. Kim, S. J. Park, K. J. Maeng, S. C. Lee, C. S. Lee, Multi-platform omics analysis for identification of molecular characteristics and therapeutic targets of uveal melanoma. *Sci. Rep.* **9**, 19235 (2019).

65. J. L.-Y. Huang, O. Urtatiz, C. D. Van Raamsdonk, G. Oncogenic, Oncogenic G protein GNAQ induces uveal melanoma and intravasation in mice. *Cancer Res.* **75**, 3384–3397 (2015).

66. A. N. Shoushtari, R. D. Carvajal, GNAQ and GNA11 mutations in uveal melanoma. *Melanoma Res.* **24**, 525–534 (2014).

67. Y. Perez-Riverol *et al.*, The PRIDE database and related tools and resources in 2019: Improving support for quantification data. *Nucleic Acids Res.* **47**, D442–D450 (2019).

68. G. B. Phelps, H. R. Hagen, A. Amsterdam, J. A. Lees, MITF deficiency accelerates GNAQ-driven uveal melanoma. Gene Expression Omnibus. https://www.ncbi.nlm.nih.gov/geo/query/acc.cgi?acc=GSE190802. Deposited 13 December 2021.

69. G. B. Phelps, H. R. Hagen, A. Amsterdam, J. A. Lees, MITF deficiency accelerates GNAQ-driven uveal melanoma. ProteomeXchange Consortium via PRIDE. https://www.ebi.ac.uk/pride/archive/projects/PXD030527. Deposited 19 December 2021.